Enhancing detection of volcanic ash clouds from space with convolutional neural networks

Federica Torrisi [a,b], Claudia Corradino [a,*], Simona Cariello [a,b], Ciro Del Negro [a]

[a] *Istituto Nazionale di Geofisica e Vulcanologia, Sezione di Catania, Osservatorio Etneo, Catania, Italy*
[b] *Dipartimento di Ingegneria Elettrica Elettronica e Informatica, University of Catania, Catania, Italy*

A R T I C L E   I N F O

A B S T R A C T

Volcanic ash cloud detection is a crucial component of volcano monitoring and a valuable tool for investigating ash cloud dispersion, which is paramount for enhancing the safety of human settlements and air traffic. The latest generation of high-resolution satellite sensors (e.g., EUMETSAT MSG Spinning Enhanced Visible and InfraRed Imager, SEVIRI) provides radiometric estimates for monitoring volcanic clouds on a global scale efficiently and timely. However, these radiometric intensities are not always discriminative enough to detect volcanic ash clouds due to the spectral limitations of these instruments and the complex nature of some volcanic clouds, such as low concentration resulting in an averaged detected radiometric estimate comparable to the background. Here, we evaluate the ability of a Convolutional Neural Network (CNN) to detect and track the dispersion of volcanic ash clouds into the atmosphere, exploiting a variety of spatial and spectral intensity information mainly coming from SEVIRI Ash RGB images. We train a deep CNN model through transfer learning, and demonstrate that the trained models overcome the limitations of algorithms based solely on pixel intensity, whether traditional or machine learning, resulting in increased performance compared to other methods. We illustrate the operation of this model using the paroxysmal explosive events that occurred at Mt. Etna between 2020 and 2022.

1. Introduction

Volcanic ash clouds are generated by violent explosive eruptions, releasing hot silicate fragments called pyroclasts and volcanic gases (Self, 2006). They can rise to heights of up to 50 km as heat is transferred from the hot pyroclasts to entrained air from the surrounding atmosphere (Gilbert and Sparks, 1998; Pyle, 1998). Once aloft, they can drift for thousands of kilometers from the eruptive vent, depending on wind speed and the wind shear, and can persist in the atmosphere for an extended period. Common components found in a volcanic cloud include ash particles, tiny fragments of volcanic rocks and mineral crystals, and gases such as water vapor, sulfur dioxide (SO_2), and carbon dioxide (CO_2) (Durant et al., 2009; Hunton et al., 2005). These components can pose various hazards to both the environment and human health. Ash particles released into the atmosphere can damage aircraft engines, impact the human respiratory system if inhaled, and affect infrastructure when heavy accumulations occur (Chen and Zhao, 2015; Gudmundsson, 2011; Wilson et al., 2012). Furthermore, a high level of SO_2 in a volcanic cloud can contribute to the formation of acid rain when SO_2 combines with water vapor and may cause acute respiratory

symptoms among people living near an active volcano (Ishigami et al., 2008; Williams-Jones and Rymer, 2015). Observing and tracking volcanic clouds are crucial to enhance the safety of human settlements and air traffic.

Nowadays, Earth Observation (EO) sensors onboard orbiting satellites are the primary means widely used by operational monitoring centers, such as the Etna Volcano Observatory (EVO), to forecast the movement of volcanic ash clouds. However, to accomplish this, they first need to know that an eruption has occurred (Pavolonis et al., 2018; Scollo et al., 2009; Webley et al., 2009). The detection of volcanic clouds involves identifying the areas affected by the presence of volcanic ash and gases emitted during a volcanic eruption. Sawada (1987) was the first to investigate volcanic clouds using satellite images, although the detection rate was quite low, probably due to the interference from meteorological clouds and the limitations of the instruments of that time (Sawada, 1996). Automatically detecting volcanic clouds using satellite remote sensing data is challenging yet crucial due to their potential impact on aviation, human health, and the environment. In this context, an automatic detection model with high accuracy is essential for identifying volcanic clouds band retrieving important information such as

---

Volcanic Cloud Top Height, their components (ash, SO_2, ice, etc.) and their quantities, spread direction, and distance covered.

Classical methods for detecting volcanic clouds rely on establishing thresholds to discriminate pixels within a volcanic cloud. The widely used technique, known as the "Brightness Temperature Difference" (BTD), was developed by Prata (Prata, 1989a, 1989b). This method is based on the difference between the brightness temperature (BT) of two images acquired at slightly different wavelengths within the 8 to 12 μm range of the infrared spectrum. Volcanic ash clouds predominantly consist of silicate particles, and their interaction with infrared radiation differs from that of ice and water, the primary components of conventional meteorological clouds. Specifically, in the presence of volcanic ash, the BT measured above the ash cloud increases as the wavelength extends in the infrared region of the electromagnetic spectrum, resulting in negative values of BTD. Conversely, this trend reverses for layers of ice or water particles, commonly found in meteorological clouds, leading to positive values of BTD. This method is also called "Reverse Absorption" due to this characteristic. However, in cases of mixtures, the capability to distinguish between components diminishes proportionally, and, in some cases, becomes ineffective, such as when ash particles are entirely enveloped by ice (Rose et al., 1995).

The evolution of machine learning (ML) has significantly enhanced its potential as a powerful tool for developing automatic models to detect volcanic clouds. ML algorithms have become more sophisticated and versatile, enabling complex pattern recognition and feature extraction (Amato et al., 2022; Corradino et al., 2021). Over the last decade, various ML techniques have been applied to detect volcanic clouds using satellite data. For instance, a neural-network-based model was applied to Sentinel-3 SLSTR (Sea and Land Surface Temperature Radiometer) to detect volcanic ash plumes (Petracca et al., 2022). Additionally, supervised techniques like support vector machines (SVM) have proven effective for this task. SVMs perform well in high-dimensional feature spaces and are less prone to overfitting, making them advantageous when dealing with limited labeled data (Torrisi, 2022; Torrisi et al., 2022). ML models can be implemented for real-time monitoring of volcanic cloud detection, providing timely alerts for aviation safety and hazard assessment. For example, VACOS (Volcanic Ash Cloud properties Obtained from SEVIRI) is a new retrieval algorithm that utilizes SEVIRI (Spinning Enhanced Visible and Infrared Imager) data and artificial neural networks to identify volcanic clouds and retrieve parameters such as mass column concentration, cloud top height, and the effective particle radius (Piontek et al., 2021).

ML approaches have demonstrated promise in detecting volcanic clouds due to their ability to learn complex patterns from data. Supervised ML requires large, high-quality labeled datasets for training, which can be challenging to obtain due to the relatively infrequent occurrence of volcanic eruptions. Additionally, volcanic cloud detection datasets can be highly imbalanced, with a small number of positive examples (volcanic cloud) and a large number of negative examples (non-volcanic cloud or background). Imbalanced datasets can lead to biased model predictions, favoring the majority class while neglecting the minority class. Thus, specialized techniques are required to address the imbalance (Dempsey et al., 2022; Ardid et al., 2023). Effective feature engineering may also be necessary to extract relevant information from remote sensing data, although this process can be time-consuming. From this perspective, deep learning (DL) enables the development of deep neural networks capable of learning intricate relationships in data, reducing the need for manual feature engineering (Amato et al., 2023). DL models can capture local spatial and higher order features crucial for detecting subtle volcanic features in imagery. Recently, we successfully applied Deep Convolutional Neural Networks (CNNs) to ASTER satellite thermal images, allowing us to learn volcanic spatial local features and detect subtle volcanic thermal anomalies comparable in intensity with the background (Corradino et al., 2023). These techniques typically require a huge volume of labeled data when trained from scratch. However, a pre-trained deep learning model trained on large datasets to accomplish a specific task and can be fine-tuned for another task, i.e. the weights learned by the pre-trained model are used as starting values for training a new model. This technique, called transfer learning, leverages knowledge learned from vast datasets to improve model performance with limited labeled data. Nonetheless, DL presents some limitations, such as the complexity of the model architecture and its black box nature, meaning that the models yield output without explicitly revealing the underlying decision-making process. This complexity makes interpretability difficult (Li et al., 2022). Nevertheless, different approaches have been proposed to enhance CNN interpretability (Zhang et al., 2018).

Here, we developed a new deep learning segmentation model to improve the accuracy of volcanic cloud detection in satellite images. Image segmentation involves partitioning an image into multiple coherent regions, commonly used for identifying objects and boundaries. Our model is a hybrid of U-Net (Shelhamer et al., 2017) and VGG16 (Simonyan and Zisserman, 2014), incorporating transfer learning to simplify the U-Net architecture, thus speeding up training and reducing computing resources. This hybrid model is tailored to process and analyze SEVIRI Ash RGB images. After training on labeled images and validation on new data, it can be applied to any new SEVIRI Ash RGB image. We implemented this model using Google Colab, a cloud-based platform facilitating the deployment of models on distributed computing resources, ideal for processing large datasets efficiently. Subsequently, we applied the model to analyze a long sequence of paroxysmal events at Mt. Etna volcano (Italy) between 2020 and 2022.

2. Satellite data

The Spinning Enhanced Visible and Infrared Imager (SEVIRI) is a pivotal instrument aboard the geostationary weather satellite Meteosat Second Generation (MSG), managed by the European Organization for the Exploitation of Meteorological Satellites (EUMETSAT). Operating from a geostationary orbit, SEVIRI is a multispectral imaging radiometer that furnishes continuous, high-resolution observations of the Earth's atmosphere and surface. Its primary mission is to monitor weather and climate-related phenomena across Europe and Africa. SEVIRI captures data across various spectral bands, including visible, near-infrared, and infrared wavelengths. With 12 spectral channels covering a broad range of wavelengths, it facilitates the observation of diverse meteorological and environmental features. SEVIRI delivers high spatial resolution images, with a pixel size of approximately 3 km at the sub-satellite point. Continuously scanning the Earth's full disk, SEVIRI captures images every 15 min in both the visible and infrared spectra (Aminou, 2002).

Access to SEVIRI images is facilitated through the EUMETSAT API in Python, enabling interaction with the EUMETSAT Data Store. This interface empowers users to search for products based on collections and apply filters based on data attributes, region of interest, timeliness, and coverage. Specifically, we utilized the MSG Level 1.5 Image Data product, which encompasses image data corrected for all undesired radiometric and geometric effects, geolocated using a standardized projection, and calibrated and radiance-linearized. The Level 1.5 images, provided in a geostationary projection (GEOS Projection), were georeferenced to the EPSG:4326—WGS 84 reference system.

3. Methods

Image segmentation, a fundamental field in computer vision, aims to group similar regions of an image into distinct class labels, extending beyond simple classification to precisely delineate the object boundaries. A basic segmentation technique is thresholding, which categorizes pixels into two classes based on a predefined threshold. Pixels above the threshold are assigned one class (often represented as 1), while those below the threshold are assigned the other (typically represented as 0). Thresholding is particularly effective when there is a clear difference in pixel values between the two classes, allowing for straightforward

selection of the threshold. However, its performance can be limited in scenarios where manual selection of threshold values is required. To overcome this limitation and automate the threshold selection process, machine learning can be employed. Previously, we developed a Support Vector Machine (SVM) model for automatically detecting volcanic clouds using SEVIRI Ash RGB images, relying on spectral characteristics of the data. However, this approach may mistakenly classify parts of meteorological clouds as volcanic clouds due to spectral similarities. To address this issue, Convolutional Neural Networks (CNNs) provide a valuable solution. Their ability to automatically learn spatial hierarchies of features from data enhances their accuracy in discriminating complex patterns, such as distinguishing between volcanic and meteorological clouds. Even when spectral characteristics are closely matched, CNNs excel in identifying subtle spatial differences, making them advantageous for accurate cloud classification.

We have developed a hybrid DL algorithm in Google Colab to automatically detect and recognize the volcanic ash clouds from SEVIRI Ash RGB images. This approach utilizes thermal infrared satellite observations not only for detecting volcanic clouds based on the presence of thermal anomalies at a specific time, but also for identifying numerous volcanic features based on their thermal and geometric characteristics. After training the model on labeled samples and validating its performance on new images, it can be applied to new unlabeled images. Its ability to generalize and make predictions on unseen data makes it suitable for near real-time monitoring of volcanic clouds. Our schematic framework involves three main steps: (a) Input Features Preparation, (b) Segmentation, and (c) Performance Evaluation, as illustrated in Fig. 1. These three steps are described in more detail below.

3.1. Input feature preparation

We collected SEVIRI images of Sicily, covering the area from 36.5 to 39.5 degrees north latitude and from 12 to 18 degrees east longitude. This region encompasses Mt. Etna and its surrounding areas, which are frequently affected by volcanic clouds following explosive eruptions. We used SEVIRI Ash RGB images as input features of the proposed hybrid architecture. The SEVIRI Ash RGB image is an RGB (Red, Green, Blue) composite created by combining the IR8.7, IR10.8, and IR12.0 channels. This combination produces a false-colour image that highlights the presence of volcanic ash and sulfur dioxide (SO_2) resulting from volcanic eruptions. The construction of this product involves combining the brightness temperature (BT) of the three SEVIRI thermal infrared (TIR) channels and enhancing each channel within specific BT ranges (EUMETSAT SEVIRI Ash RGB Guide). An Ash RGB image is obtained as follows:

- Red Channel: $BT_{12.0} - BT_{10.8}$ (range [−4 K, +2 K]);
- Green Channel: $BT_{10.8} - BT_{8.7}$ (range [−4 K, +5 K]);
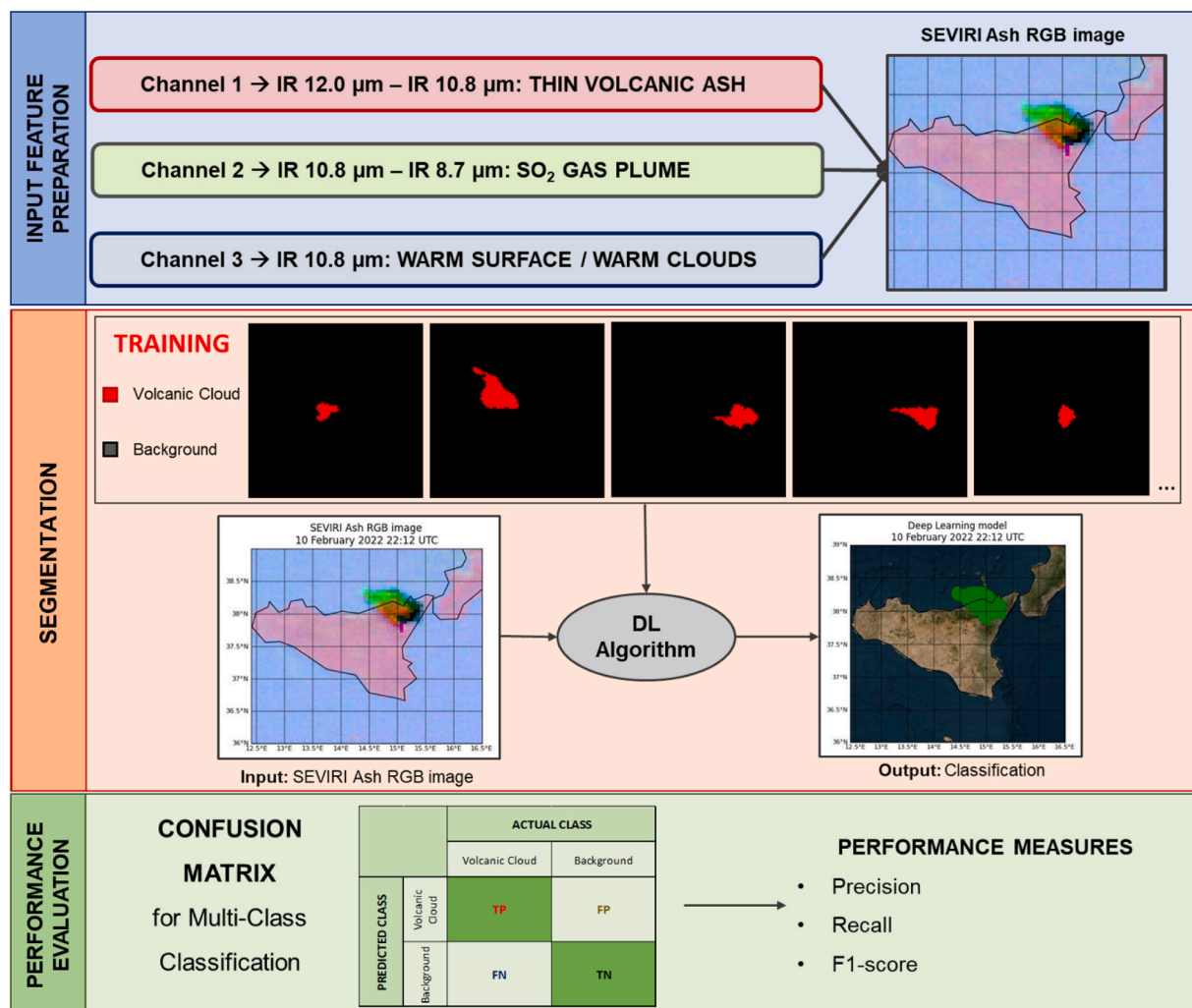- Blue Channel: $BT_{10.8}$ (range [243 K, 303 K]).

Fig. 1. General scheme representing the three main steps of the hybrid deep learning (DL) algorithm: (a) Input Features Preparation, (b) Segmentation and (c) Performance Evaluation.

The red channel is particularly effective for ash detection, utilizing the inverse of the "reverse absorption" method. This means that the Brightness Temperature Difference (BTD) is negative for thin ice clouds and positive for thin ash clouds. Consequently, thin volcanic ash tends to exhibit a strong reddish colour, while meteorological clouds contribute minimally. The green channel highlights the presence of SO_2 by comparing the SO_2 absorption band at 8.7 μm with the non-absorbing 10.8 μm band. Lastly, the 10.8 μm channel in the blue spectrum provides a high contrast background for ash detection and eliminates the influence of cumulonimbus clouds. In summary, areas of volcanic ash clouds generally appear red when little SO_2 is present and yellow when significant SO_2 is present. In the absence of ash, SO_2 appears green.

To enhance the visual discrimination of different features within a SEVIRI Ash RGB image, we applied decorrelation stretch. This technique removes the high correlation commonly found in multispectral datasets to produce a more colorful composite image. The decorrelation stretch process requires three bands for input and is based on three main steps (Campbell, 1996):

- The original bands are first transformed into their principal components;
- The transformed variables are then stretched separately;
- The inverse of the principal component transformation is applied.

Each image initially has dimensions 100x100x3 and is then resampled to 500x500x3 to match the input dimensions required by our architecture. These images are then saved in PNG format and are ready for use by the DL model. Training and testing datasets are created by gathering images containing extended volcanic clouds with characteristic shapes, as it is crucial to include representative samples of the object we aim to segment. The eruptive events at Mt. Etna considered for the training and testing datasets are as follows: 21 February 2021, 22 February 2021, 28 February 2021, 4 March 2021, 12 March 2021, 9 August 2021, 10 February 2022, and 21 February 2022. Detailed description of these eruptive episodes are provided in our precedent work (Torrisi et al., 2023). A comprehensive list of all 66 paroxysms occurring at Mt. Etna between 2020 and 2022 is described by Calvari and Nunnari (2022). For each event, the ratio between training and testing images remains consistent: 70% for training and 30% for testing, with images randomly selected for both sets. Additionally, we adopt data augmentation techniques to increase the size of the training dataset, appling random transformations such as image rotation, flipping, and skew to existing data (van Dyk and Meng, 2001). Consequently, the proposed hybrid architecture is trained on a set of 372 SEVIRI Ash RGB images and then applied to 65 SEVIRI Ash RGB images. Table 1 displays the number of training and testing images for each explosive event. Ground truth images are obtained by meticulously labeling SEVIRI Ash RGB images through visual inspection, indicating the true class of each pixel. In this case, it is a binary classification, with the two classes being "volcanic cloud" or "background". For the training dataset, we choose to use a sequence of images related to several volcanic explosive eruptions of Mt. Etna occurring between 2020 and 2022. The selection of test images is made to include volcanic clouds resulting from various eruptions of Mount Etna occurring during different non-consecutive periods within the timeframe of 2020 to 2022.

3.2. CNN architecture: UNet-VGG16

A Fully Convolutional Network (FCN) is a type of convolutional neural network (CNN) architecture designed for pixel-level tasks, particularly in the domain of image segmentation. It employs only locally connected layers, such as convolution, pooling, and upsampling. FCN can work for variable image sizes, as long as all connections remain local. By not incorporating dense layers, the network benefits from a reduction in parameters, leading to a faster training process. Hence, an FCN has the capability to classify every pixel within an image, and its

Table 1

SEVIRI Ash RGB images used to build the training and testing dataset. For each event, the series of images between the start date and the end date is considered. The last two columns of the table represent the total number of images used for the training and testing phase, respectively, after the application of the Data Augmentation technique.

Event	Start date	End date	N° training images (with DataAug)	N° testing images
21 February 2021	21 February 2021 00:12 UTC	21 February 2021 04:57 UTC	72	8
22 February 2021	22 February 2021 23:27 UTC	23 February 2021 02:57 UTC	102	12
28 February 2021	28 February 2021 07:42 UTC	28 February 2021 10:57 UTC	42	6
4 March 2021	4 March 2021 07:57 UTC	4 March 2021 12:27 UTC	60	8
12 March 2021	12 March 2021 07:57 UTC	12 March 2021 11:57 UTC	60	6
9 August 2021	9 August 2021 03:27 UTC	9 August 2921 04:27 UTC	0	8
10 February 2022	10 February 2022 22:12 UTC	10 February 2022 23:12 UTC	0	13
21 February 2022	21 February 2022 12:27 UTC	21 February 2022 15:27 UTC	36	4
		Total	372	65

architecture comprises two main blocks: an encoder and a decoder. The encoder path reduces the input matrix size by increasing the number of feature maps, whereas the decoder path restores the matrix to its original size while minimizing the number of feature maps, so that the segmentation results can be compared with the ground truth at each pixel. In this work, we use the U-Net as an FCN architecture. It was first designed and applied in 2015 for processing biomedical images (Ronneberger et al., 2015). In biomedical cases, the focus is not only to distinguish whether there is a disease but also to localize the area of abnormality. For this reason, U-Net is popular for fast and precise segmentation of images. It is a U-shaped encoder-decoder network architecture, which consists of four encoder blocks and four decoder blocks that are connected via a bridge: input images are fed into an encoder architecture to capture high-level contextual information, which is subsequently transmitted to a decoder architecture to recover spatial details and generate pixel classification results (Tomar, 2021; Weng et al., 2019). Due to its complexity, the U-Net architecture can require a significant amount of time for execution. To address this challenge, a new model combining the U-Net architecture with VGG16 is proposed. This aims to reduce the complexity of U-Net and to speed up the execution times. The encoder block of the U-Net is replaced with a VGG16 due to its similarity to U-Net's encoder path, the smaller number of parameters, and the easy accessibility to parameter weights, which are used in the new model (Kanaeva and Ivanova, 2021).

VGG16, also known as VGG-Net, is a convolutional neural network with 16 layers (three fully connected layers and 13 convolutional layers). It is a relatively extensive network with a total of 138 million parameters, but its simplicity is its main attraction (Simonyan and Zisserman, 2014). The model achieves 92.7% top-5 test accuracy in ImageNet, which is a dataset of over 14 million images belonging to 1000 classes. It replaces large kernel-sized filters with multiple 3 × 3 kernel-sized filters one after another. A general scheme of the proposed model is shown in Fig. 2.

3.3. Training

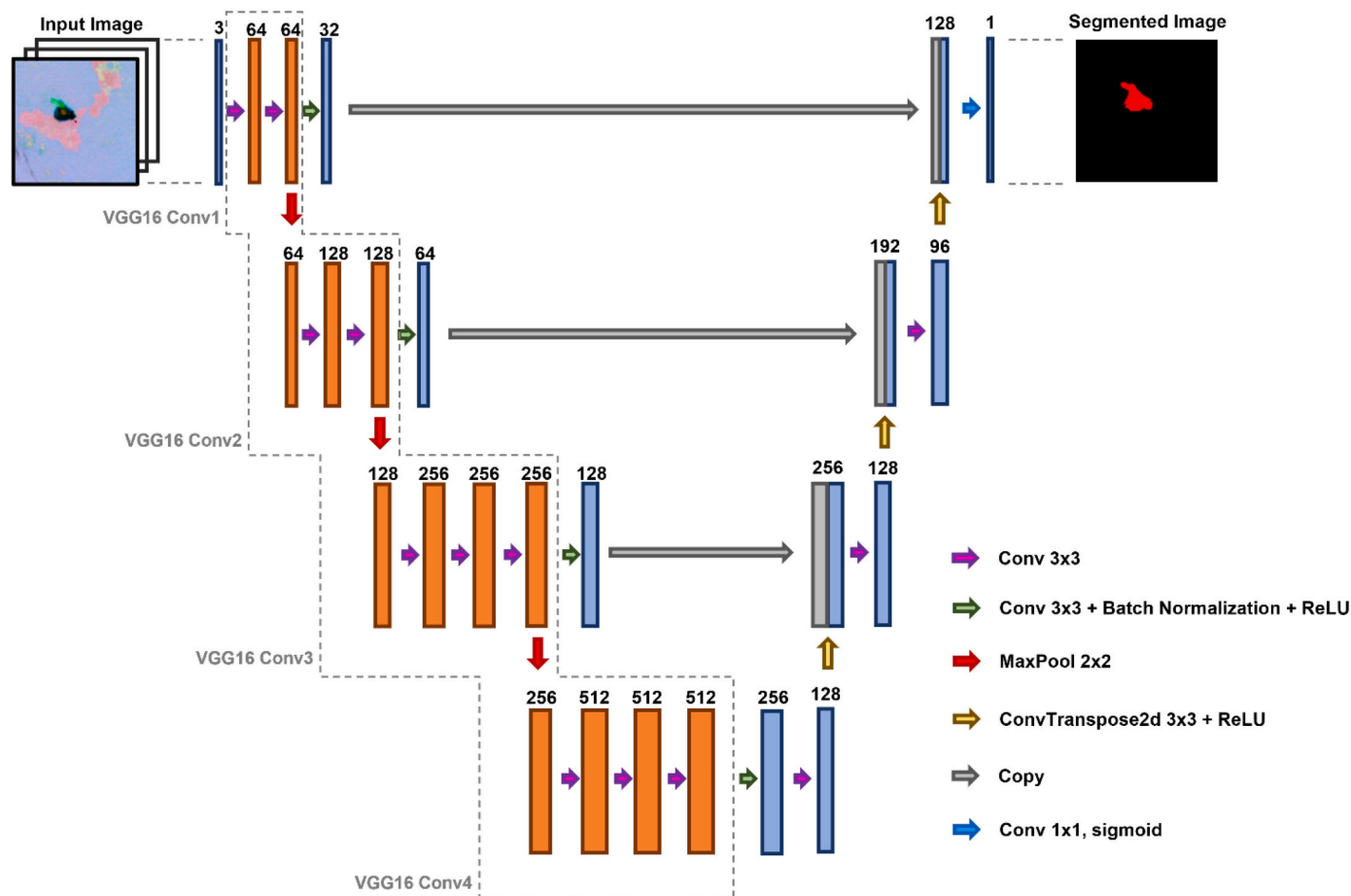Instead of training from scratch, we adopt transfer learning to

Fig. 2. VGG16 + UNet architecture is a deep learning hybrid architecture that combines a VGG16 model, renowned for its reduced complexity and use of a smaller number of parameters, with the UNet, which excels particularly in the domain of image segmentation.

enhance the accuracy of the output, saving training time and requiring less training data. Transfer learning is a popular approach in deep learning, where pre-trained models developed for a specific task serve as the starting point for computer vision and natural language processing tasks. This is primarily due to the significant computational and time resources required to develop neural network models in these domains.

The VGG16 model, initially trained on the ImageNet dataset, utilizes its pre-trained layers for feature extraction. We implement the freezing of convolutional layers, preventing the weights of these frozen layers from being updated during backpropagation. Additionally, we set the pooling layers to trainable mode to fine-tune the pre-trained model. This means that the weights of these layers are updated during back-propagation, allowing the adjustment of the pre-trained model with respect to the new dataset and aiming to achieve the best possible result.

The proposed hybrid VGG16-UNet model has been trained with a learning rate of 0.001. The Adaptive Moment Estimator (Adam) optimizer (Kingma and Ba, 2017) is utilized to minimize the focal loss, an improved version of the cross-entropy (CE) loss based on the Down Weighting technique, which reduces the influence of easy example on the loss function, ensuring that predictions on hard examples improve over time rather than becoming overly confident with easy ones (Nayak, 2022). Thus, focal loss aims to address the class imbalance problem typically affecting satellite image segmentation tasks (Corradino et al., 2023), which may still be present because many volcanic clouds occupy a very small portion of the image compared to the background.

3.4. Testing and performance evaluation

The trained model is then applied to testing images, defined as out-

of-sample since they were not seen during the training phase. To assess the performance of the model, we constructed a confusion matrix and evaluated various performance indices. For binary classification, the confusion matrix is a 2×2 table that compares the actual target values with those predicted by the ML model. The confusion matrix consists of four components:

- True positives (TP): the number of real positives correctly predicted as positive;
- True negatives (TN): the number of real negatives correctly predicted as negative;
- False positive (FP): the number of real negatives wrongly predicted as positive;
- False negative (FN): the number of real positives wrongly predicted as negative.

Precision and recall are two important performance metrics for binary classification obtained from the confusion matrix, where precision measures the accuracy of the positive predictions made by the model. High precision means that when the model predicts a positive class, it is likely to be corrected.

$$precision = \frac{TP}{TP + FP}$$

Recall, also known as sensitivity and true positive rate, measures how well the model correctly identifies all positive instances. High recall indicates that the model is effective at finding positive instances.

$$recall = \frac{TP}{TP + FN}$$

Traditional performance metrics like accuracy can be misleading when dealing with unbalanced datasets, since they tend to be biased towards the majority class. A model that predicts the majority class for all instances may achieve high accuracy, but it provides little value if it fails to detect the minority class. Therefore, since the background class contains a significantly greater number of pixels compared to the volcanic cloud class (i.e., an unbalanced dataset), we need to use performance indices to address this problem. The F1-score is a good performance metric for unbalanced datasets. The F1 score assesses the predictive skill of a model by elaborating on its class-wise performance rather than an overall performance, as done by accuracy. It combines the precision and recall scores of a model.

$$F1 = \frac{2TP}{2TP + FN + FP}$$

F1-score gives equal importance to precision and recall, making it useful when aiming to strike a balance between correctly identifying the minority class (recall) and avoiding false positives (precision).

3.5. Comparison with existing methods

We compared the outcomes of our proposed DL model with the results of other techniques existing in the literature: the classical Brightness Temperature Difference (BTD) approach and the support vector machine (SVM). The BTD approach involves taking the difference between two bands and setting an appropriate threshold: pixels with values below the threshold are categorized as "volcanic cloud", while those exceeding this threshold are considered "background". In SEVIRI data, the BTD image is generated by computing the difference between the IR band at 10.8 μm and the IR band at 12.0 μm, with a selected detection threshold (DT) set to 0 K (Prata, 1989a). However, BTD is sensitive to variations in atmospheric conditions, such as water vapor content and cloud cover, which can introduce noise and affect the accuracy of the detection (F. Prata and Lynch, 2019). Moreover, BTD primarily focuses on temperature differences and lacks spatial information, making it less suitable for tasks like precise volcanic cloud tracking and segmentation. On the other hand, SVM is a supervised machine learning algorithm with the goal of finding the optimal hyperplane or set of hyperplanes that best separates data points into different classes. We used an SVM classifier with a radial basis function as a kernel, the spread of the kernel (γ) set to 0.5 and the cost parameter set to 10. This model was trained on samples of SEVIRI Ash RGB images, labeled as "volcanic cloud" or "background", and was tested on new

SEVIRI Ash RGB images, showing good accuracy (Torrisi et al., 2022).

The results from these different methods are going to be compared with the outcomes of the DL model. We constructed a confusion matrix for each method and then calculated the precision, recall, and F1-score, which are the primary evaluation metrics.

4. Results

The VGG16-UNet model was tested on a dataset of 65 images, defined as out-of-sample since they were not seen during the training phase. For simplicity, we show the results of the application of the model to three out-of-sample images related to the events occurred at Mt. Etna on 23 February 2021, 9 August 2021, and 10 February 2022 (respectively in Figs. 3, 4, and 5). For each case, we present the SEVIRI Ash RGB image (Figs. 3a, 4a, and 5a) used as input of the model, the ground truth labels (Figs. 3b, 4b, and 5b) and the corresponding segmented outcome (Figs. 3c, 4c, and 5c). The SEVIRI AshRGB image in Fig. 3a shows the volcanic cloud produced during the event of the 23 February 2021, which is mainly composed of SO2 (green pixels) and is moving north west. The volcanic clouds in Fig. 4a and 5a are characterized mainly by ash (red pixels), SO2 (green pixels) and both the components (yellow pixels).

From these three illustrative cases, it becomes evident that the proposed VGG-16 model performs effective segmentation of volcanic clouds in SEVIRI Ash RGB images. The model demonstrated its capability to detect all the three volcanic clouds, even with different components such as SO2, ash, and ice. The first is primarily characterized by SO2 and ice, the second by SO2 and ash, while the last encompasses all these components. Considering the ground truth as a reference, there are instances where the model tends to classify more pixels as volcanic clouds, resulting in a higher number of false positives. In the presence of thin meteorological clouds, as observed in the bottom-left part of Fig. 3a, the model exhibits proficiency in discriminating them accurately (Fig. 3c). However, occasional misclassifications occur, as seen in Fig. 4c, where certain parts of thick meteorological clouds are erroneously labeled as volcanic clouds.

The accuracy of the proposed VGG16-UNet model was computed using precision, recall and F1-score as performance indices. A confusion matrix was constructed by comparing the model's predictions with the actual ground truth labels for all testing images (see Table 2 for the confusion matrix of the model with focal loss).

Once the confusion matrix is obtained, the performance metrics (precision, recall and F1-score) are calculated. To evaluate the performance of the proposed model using focal loss, a comparison with a model using standard cross-entropy (CE) and the same settings is shown in Table 3.
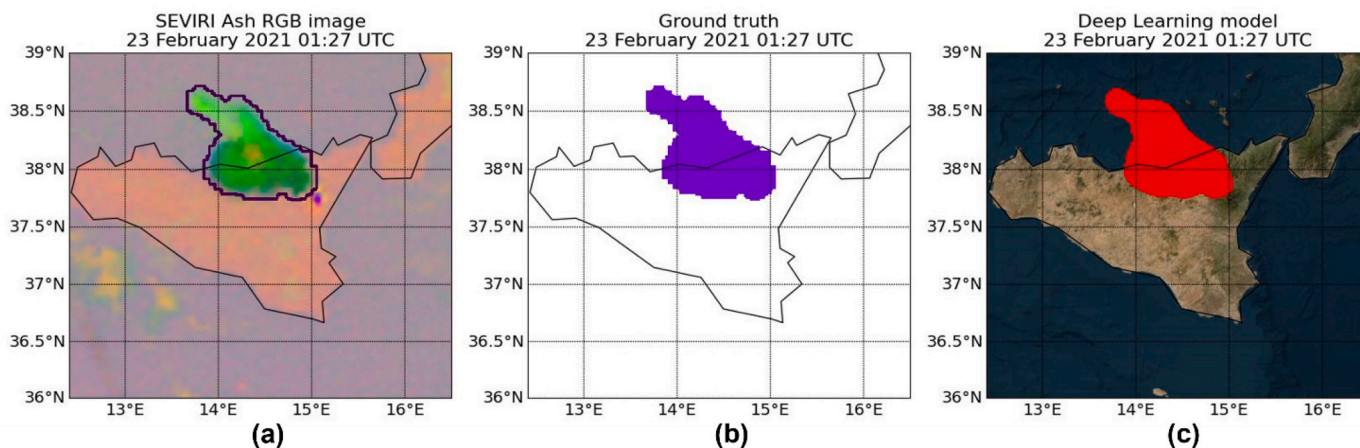

Fig. 3. Volcanic cloud produced during the event occurred at Mt. Etna on 23 February 2021 at 01:27 UTC. (a) SEVIRI Ash RGB Image, (b) Ground truth, (c) Output of the deep learning model.
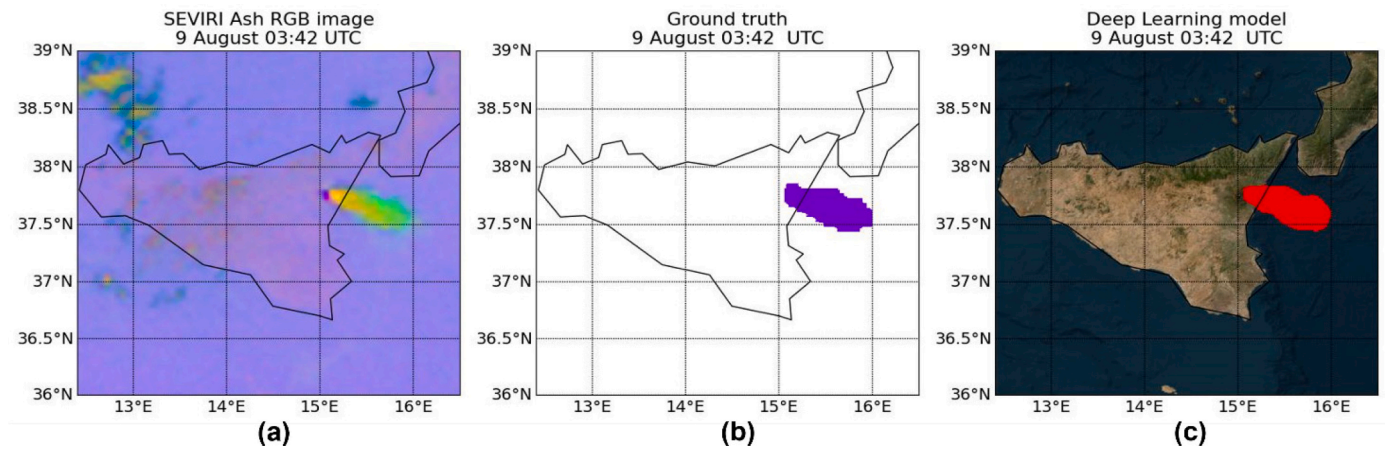
Fig. 4. Volcanic cloud produced during the event occurred at Mt. Etna on 9 August 2021 at 03:42 UTC. (a) SEVIRI Ash RGB Image, (b) Ground truth, (c) Output of the deep learning model.
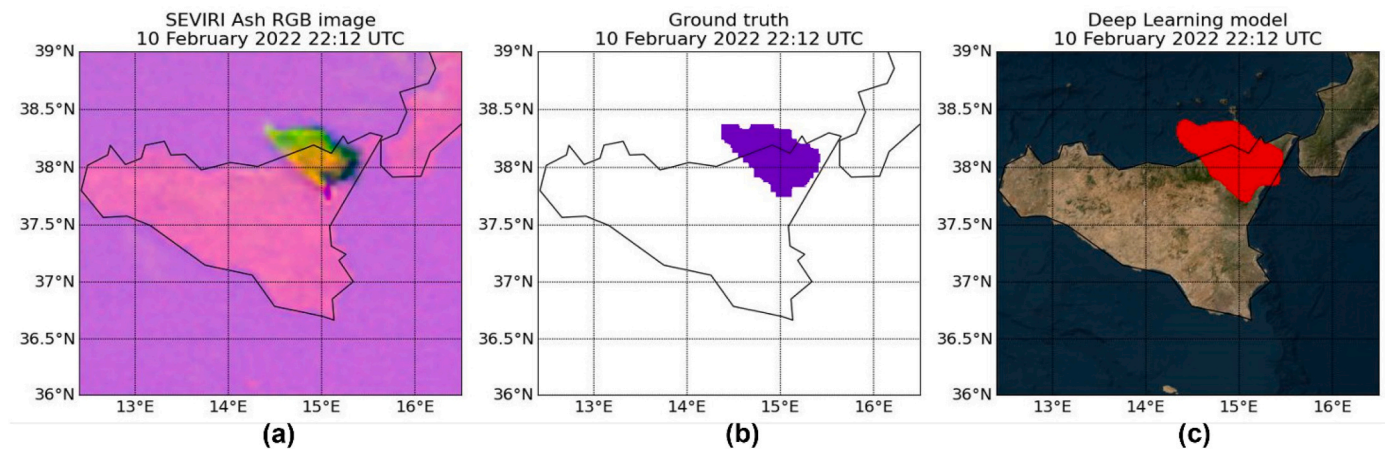

Fig. 5. Volcanic cloud produced during the event occurred at Mt. Etna on 10 February 2022 at 22:12 UTC. (a) SEVIRI Ash RGB Image, (b) Ground truth, (c) Output of the deep learning model.

Table 2
Confusion matrix calculated on the 65 testing images (79.61e5 samples) with percentage values.

		Actual values	
		Volcanic cloud	Background
Predicted values	Volcanic cloud	2.2e5 (89%)	0.01e5 (0.5%)
	Background	0.8e5 (11%)	76.6e5 (99.5%)

Table 3
Performance indices.

	Cross-Entropy	Focal Loss
Precision	0.29	0.88
Recall	0.90	0.91
F1-score	0.74	0.90

We applied the BTD technique, the SVM, and the VGG16-UNet model to three test images taken on 23 February 2021 at 06:12 UTC, 28 February 2021 at 08:57 UTC, and 9 August 2021 at 03:27 UTC (Fig. 6). Fig. 6a, e, and i show the SEVIRI Ash RGB images of the three reference events, used as input for the SVM and the VGG16-UNet model. In Fig. 6b, f, and l, green pixels correspond to the volcanic cloud classification by the BTD technique; the orange pixels in Fig. 6c, g, and m represent the

pixels classified by the SVM model as volcanic cloud, while the red pixels in Fig. 6d, h, and n represent the volcanic cloud classification performed by the VGG16-UNet model. The blue outline observed in the images corresponds to the actual contour of the volcanic cloud. For all the three cases depicted in Fig. 6, the BTD technique exhibits limitations in identifying all the pixels contained within a volcanic cloud. The choice of the threshold depends on different factors, such as atmospheric conditions, the presence of meteorological clouds, or the view zenith angle. A higher zenith angle produces a higher BTD threshold and vice versa. The performance indices related to the application of the BTD technique, the SVM, and the VGG16-UNet models to the three events of Fig. 6 are calculated and displayed in the histograms of Fig. 7. Fig. 7a, b, and c correspond, respectively, to the events of 23 February 2021 at 06:12 UTC, 28 February 2021 at 08:57 UTC, and 9 August 2021 at 03:27 UTC.

Finally, since the BTD technique cannot be automatically applied to different case studies, we did not include it as a comparison method for evaluating the overall performance across the entire dataset. Therefore, we solely applied the SVM model to the testing dataset and quantified its performance by calculating precision, recall, and F1-score (Table 4).

5. Discussion

5.1. VGG16-UNet model performance

The hybrid architecture demonstrates high performance levels,
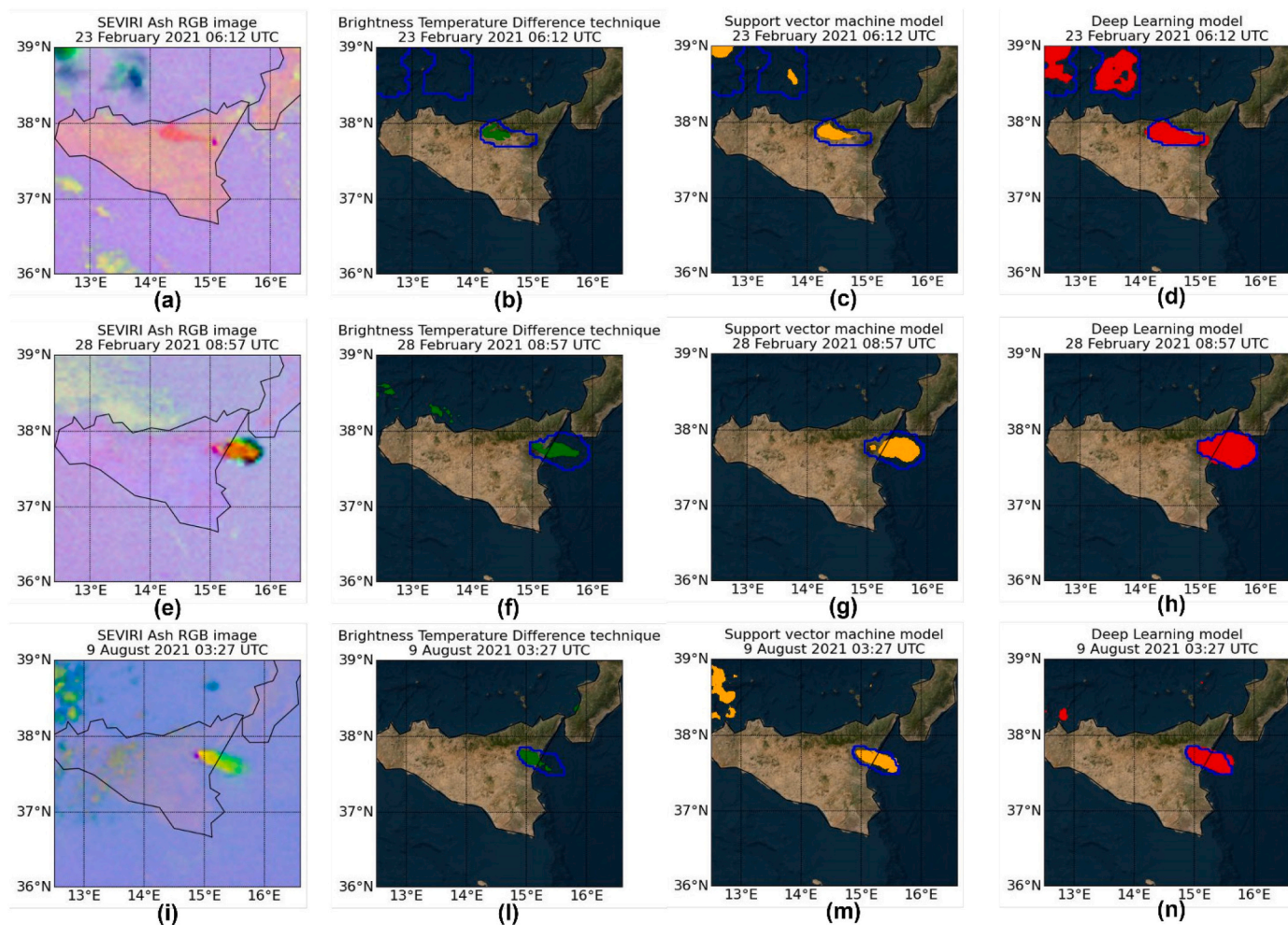
Fig. 6. Comparison between the detection capability of the brightness temperature difference (BTD) technique, the SVM and the VGG16-UNet model, for the event of 23 February 2021 at 06:12 UTC, the 28 February 2021 at 08:57 UTC, and the 9 August 2021 at 03:27 UTC. The blue outline observed in the images corresponds to the actual contour of the volcanic cloud. (For interpretation of the references to colour in this figure legend, the reader is referred to the web version of this article.)
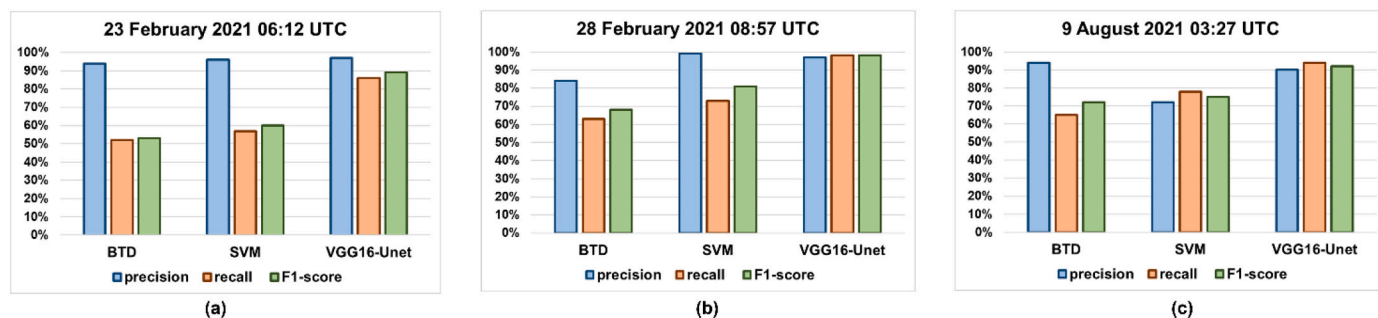

Fig. 7. Histograms to compare the performance indices (precision in blue, recall in orange and F1-score in green) of the brightness temperature difference (BTD) technique, the SVM, and the VGG16-UNet model, for the events of (a) 23 February 2021 at 06:12 UTC, (b) the 28 February 2021 at 08:57 UTC, and (c) the 9 August 2021 at 03:27 UTC. (For interpretation of the references to colour in this figure legend, the reader is referred to the web version of this article.)

Table 4
Comparison of the performance indices (precision, recall, and F1-score) of the Support Vector Machine (SVM) model and the proposed VGG16-UNet model.

	Precision	Recall	F1-score
SVM	78%	71%	74%
VGG16-UNet	88%	91%	90%

achieving an average accuracy of 0.90. The various performance indices presented in Table 3 indicate that the results obtained with focal loss are superior to those obtained with cross-entropy (CE). Precision, recall and F1-score values obtained with focal loss are all above 0.85 (specifically 0.88, 0.91 and 0.90), whereas those obtained with CE are lower (specifically 0.29, 0.90 and 0.84). This suggests that focal loss is the most suitable choice as a loss function, as it effectively handles unbalanced classes. The precision for focal loss, at 0.88, is slightly lower than the recall value of 0.91. This difference primarily arises from occasional

misclassifications by the VGG16-UNet model, leading to increased false positives and a corresponding decrease in precision. Despite the presence of an unbalanced dataset, the high F1-score indicates that the model successfully balances between making positive predictions and correctly identifying relevant instances for 90% of the samples.

The VGG16-UNet model with focal loss is then considered in our analysis due to its superior performance compared to the model trained with cross-entropy and its effectiveness in handling imbalanced datasets. The image segmentation results related to the events of 23 February 2021 at 01:12 UTC, 9 August 2021 at 03:27 UTC, and 10 February 2022 at 21:57 UTC (Figs. 3, 4, and 5, respectively) exemplify the application of the model with focal loss.

5.2. Traditional versus ML versus DL techniques

We applied the BTD technique, the SVM, and the VGG16-UNet model to three test images (out-of-samples): the 23 February 2021 at 06:12 UTC, the 28 February 2021 at 08:57 UTC and the 9 August 2021 at 03:27 UTC (Fig. 6).

Analyzing the event of 23 February 2021 (Fig. 6a), volcanic clouds are recognizable in the upper left part of the image, composed mainly of ice (dark green part) and SO_2 (light green part), and another volcanic cloud predominantly composed of ash originating from the crater of Mt. Etna. The BTD technique (Fig. 6b) can effectively identify some of the pixels inside the volcanic cloud composed of ash. However, since the cloud in the upper left part is rich in SO_2 and ice, the BTD struggles to detect this particular cloud due to the fact that BTD is based on the reverse absorption phenomenon, which highlights the contrasting behaviors of volcanic ash and ice. Both the SVM and the VGG16-UNet model successfully achieve the goal of segmenting the volcanic clouds (Fig. 6c and Fig. 6d, respectively). It is evident that the SVM exhibits limitations in accurately identifying the entire SO_2 clouds in the upper left portion of the image; however, it classifies the volcanic cloud predominantly composed of ash accurately. The VGG16-UNet model demonstrates strong performance in the segmentation of both clouds. Both models are proficient at distinguishing the thin meteorological clouds in the lower-left part of the image from volcanic clouds. From Fig. 7a, it is possible to see that the precision of BTD and SVM (95% in both cases) is higher than the recall (52% and 57%, respectively) and the F1-score (53% and 60%, respectively). This typically indicates that the model is better at accurately identifying true positives while being conservative in its predictions. This means that when the system predicts a positive case, it's often correct, but it might miss some actual positive cases. Instead, the performance indices related to the VGG16-UNet model are higher than 85% (precision: 97%, recall: 86%, F1-score: 90%).

The volcanic cloud produced during the event of 28 February 2021 is shown Fig. 6e. This volcanic cloud is composed mainly of ash (red part) and SO_2 (light green part). In this case as well, the BTD technique (Fig. 6f) is able to detect the pixels in the central region of the cloud, which contains mainly ash, but not the pixels on the border because they primarily consist of SO_2 without ash. The outcomes of SVM and VGG16-Unet models are depicted in Fig. 6g and Fig. 6h, respectively. In both cases, the segmented pixels are mostly inside the actual contour of the volcanic cloud (blue contour). Also, in the previous case, the high values of precision of the BTD and the SVM (Fig. 7b, respectively 84% and 99%), compared to recall (63% and 73%, respectively) and F1-score (68% and 81%, respectively), show a clear underestimation tendency. The VGG16-UNet model exhibits strong performance metrics, with precision at 97%, recall at 98%, and an F1-score of 98%, achieving a very high level in accurately identifying volcanic clouds.

Finally, Fig. 6i shows the event of 9 August 2021, characterized by a volcanic cloud with ash and SO_2 dispersing to the southeast and some meteorological clouds in the left parts. The BTD technique (Fig. 6l) detects only the pixels mainly characterized by ash, losing more than half of the pixels inside the cloud. The VGG16-UNet (Fig. 6n) classifies with a good level of accuracy all the pixels inside the volcanic clouds, while the

SVM (Fig. 6m) fails to detect certain pixels. Especially, it is not able to detect the green pixels in the right part of the volcanic clouds, mainly characterized by SO_2. However, both the SVM and VGG16-UNet model misclassified some pixels belonging to the thick meteorological clouds in the upper-left part of the image as volcanic clouds. This situation can occur because the spectral features of meteorological clouds are sometimes similar to those of volcanic clouds. Further investigations are needed to address this problem, and one possible solution to enhance the ability of the model to distinguish between these two types of clouds is to expand the training dataset by introducing more examples of images with meteorological clouds. Based on the information presented in Fig. 7c, it is evident that the BTD tends to underestimate its predictions, due to the high precision (precision: 94%, recall 65%, F1-score: 72%). The SVM exhibits performance metrics below 80% (precision: 72%, recall 78%, F1-score: 75%), primarily due to its inability to accurately classify certain pixels containing SO_2 within the volcanic cloud. Additionally, it tends to make misclassifications by incorrectly identifying some pixels from a meteorological cloud as volcanic clouds. Finally, the VGG16-UNet model presents robust performance metrics, with the exception that, in this specific scenario, the recall (94%) is higher than both precision and F1-score (respectively 90% and 92%). This occurs because the model occasionally tends to overestimate the pixels within volcanic clouds mask, leading to an increased number of false positives.

5.3. Comparison of the Support Vector Machine (SVM) model and the VGG16-UNet model

Overall, the SVM shows good performance in detecting volcanic clouds, achieving an average accuracy of 74%. However, it sometimes tends to underestimate the segmentation of pixels in the volcanic cloud, especially when the cloud is mainly characterized by SO_2. In these cases, some pixels inside the volcanic cloud are misclassified as background. For this reason, the VGG16-UNet model is a recommended alternative, offering higher accuracy (approximately 90%) and improved performance in these specific scenarios. Both approaches may incorrectly classify meteorological clouds as volcanic clouds, but the rate of false positives is lower for the VGG16-UNet (precision: 88%) compared to the SVM (precision: 78%). Reducing the rate of false positive is a challenging yet crucial task for ensuring the effectiveness and reliability of volcanic monitoring and alert systems. The proposed VGG16-UNet model achieves a better compromise than the SVM in terms of missed detection and false alarms.

The high temporal resolution of SEVIRI allows for almost near realtime monitoring of volcanic clouds. This means that their movement and changes can be closely tracked, enabling timely responses to potential hazards. The combination of the proposed VGG16-UNet model with the high temporal resolution of SEVIRI offers the capability to observe and track a volcanic cloud from its formation during an eruption to its dispersion into the atmosphere. The revisit time of SEVIRI is 15 min (or 5 min in rapid scan mode), whereas the VGG16-UNet processing time of new images is just 1 min. This enables rapid analysis and processing of SEVIRI data, potentially facilitating near-real-time monitoring and response to volcanic events.

5.4. Tracking the volcanic cloud: from its areal extension to its velocity

The utilization of precise automatic algorithms for volcanic cloud detection facilitates the prompt retrieval of crucial information regarding its dispersion, including areal extension, localization, traveled distance, and velocity during eruptive events. In Fig. 8, the tracking of the volcanic cloud emitted during the 21 February 2022 event is depicted through three time series: the first (blue crosses) indicating volcanic cloud extension, i.e. the total number of pixels inside the detected volcanic cloud; the second (blue circles) indicating the distance traveled by the cloud; and the third (red diamonds) indicating the propagation speed of the volcanic cloud. At the bottom of the image,
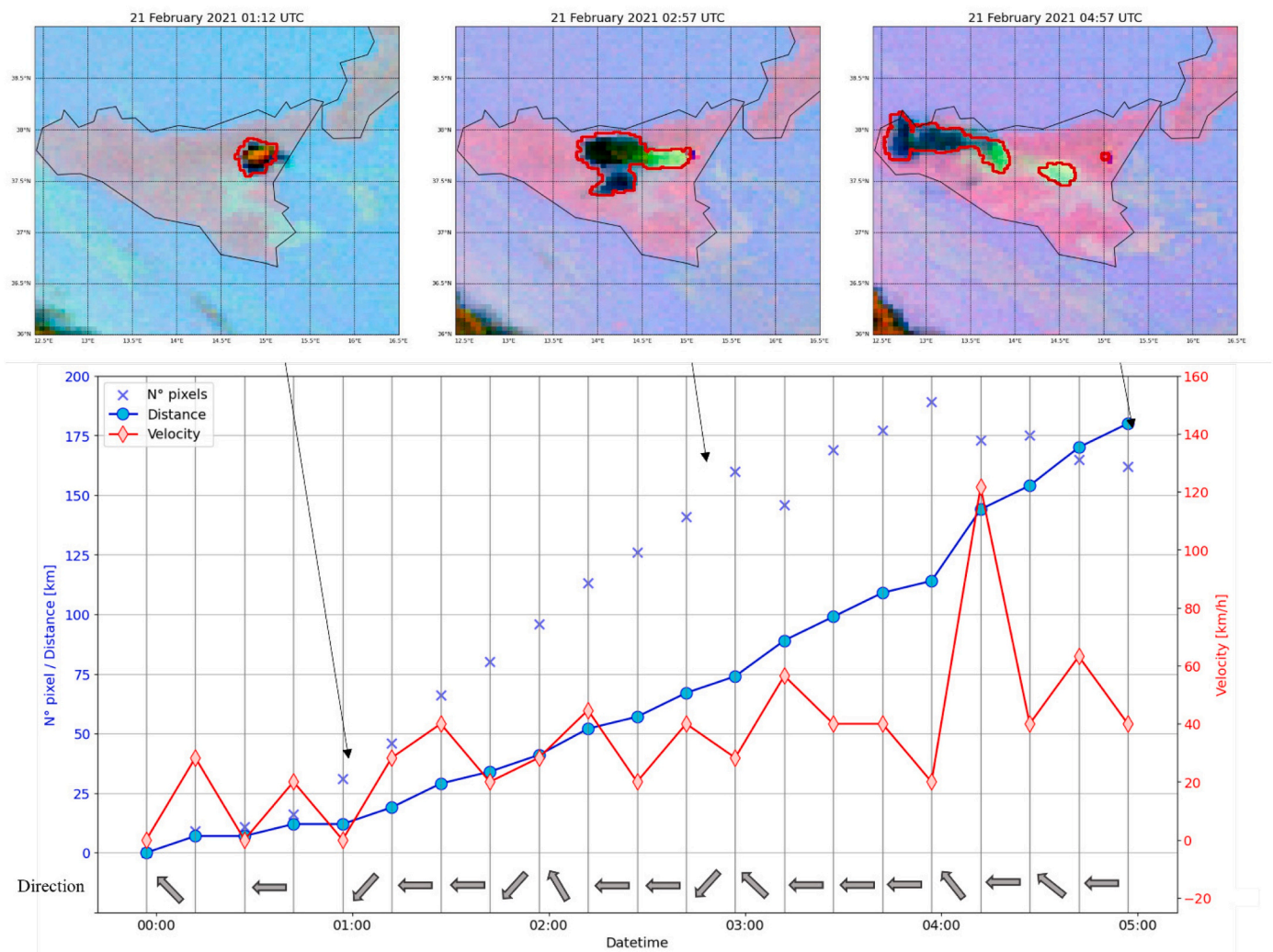
Fig. 8. Time series tracking the evolution of the volcanic cloud produced during the event on 21 February 2021: total number of pixels inside the detected volcanic cloud (blue x), distance traveled by the cloud (blue circles), and the propagation velocity of the volcanic cloud (red diamond). In the upper part, three images show different phases of the eruptive event: the inception of the volcanic cloud (21 February 2021 at 01:12 UTC), the maximum extension of the cloud (21 February 2021 at 02:57 UTC), and the dispersion of the cloud into the atmosphere (21 February 2021 at 04:57 UTC). At the bottom, arrows indicate the advection direction of the volcanic cloud. (For interpretation of the references to colour in this figure legend, the reader is referred to the web version of this article.)

arrows illustrate the advection direction of the volcanic cloud at each time step. For each image, the centroid of the identified volcanic cloud is determined, and subsequently, the Euclidean distance between the centroids of two consecutive images is calculated. These distances are then aggregated to ascertain the cumulative distance traveled by the cloud at each time step. The propagation velocity is computed as the ratio between the distance traveled at each time step and the time interval between two SEVIRI acquisitions, which is 15 min. Additionally, the advection direction of the volcanic cloud is determined at each step by calculating the angle in degrees between two centroids. This analysis was conducted considering 20 SEVIRI images acquired on 21 February 2021 (from 00:12 UTC to 04:57 UTC). Fig. 8 displays three Ash RGB images with the red contour of the volcanic cloud identified by the VGG16-UNet model. The selection of these three images was made to encompass various phases of the eruptive event: the first image captures the inception of the volcanic cloud (21 February 2021 at 01:12 UTC), the second, the moment when the cloud has expanded to its maximum extent (21 February 2021 at 02:57 UTC), and the third, when the cloud begins to disperse (21 February 2021 at 04:57 UTC). The volcanic cloud is observable from 00:12 UTC (9 pixels), and its size gradually expands until 03:57 UTC (189 pixels). Subsequently, the volcanic cloud begins to disperse into the atmosphere, resulting in a progressive decrease in the

number of pixels classified. In this sequence of 20 images from 00:12 UTC to 04:57 UTC, the volcanic cloud travels a total distance of about 175 km. This volcanic cloud is predominantly characterized by the SO_2, as evidenced by the light green pixels inside the volcanic cloud in the Ash RGB images. This component typically disperses more slowly compared to volcanic ash particles in the atmosphere. SO_2 can be transported over longer distances and remain in the atmosphere for long periods. This behavior is described by the propagation velocity of the volcanic cloud, which initially increases gradually (from 0 to 120 km/h) and then decreases after 04:12 UTC when the cloud begins to disperse into the atmosphere. Another noteworthy insight from Fig. 8 is the spread direction of the volcanic cloud. The arrows at the bottom indicate that the volcanic cloud is primarily moving towards the west. This information is valuable for evaluating the dispersion patterns of volcanic cloud materials and identifying regions potentially affected by this dispersion.

6. Conclusions

The development of a model capable of automatically detecting and tracking volcanic ash clouds in satellite images plays a crucial role in aviation safety, public health, and climate research. Leveraging the rich

spectral and spatial information embedded in satellite imagery, such a model can provide timely and accurate monitoring of volcanic activity. Particularly, the high temporal resolution of geostationary satellite sensors like SEVIRI enables near-real-time analysis, emphasizing the need for fast and efficient models for data processing.

We demonstrated the promising potential of convolutional neural networks (CNNs) in accurately identifying volcanic clouds in satellite images. The proposed hybrid architecture, VGG16-UNet, combines the strengths of VGG16 model (reduced complexity, fewer parameters, and easy access to parameter weights) with the capabilities of UNet in image segmentation. By utilizing transfer learning, we reduced training times and achieved precise segmentation of volcanic clouds in SEVIRI Ash RGB images, with a processing time of just 1 min per image. This enables rapid analysis of SEVIRI data, potentially facilitating near-real-time monitoring by processing new satellite images as soon as they are available. Compared to The VGG16-UNet model exhibits better performance Compared to traditional threshold-based approaches like BTD and classical machine learning techniques such as SVM, the VGG16-UNet model demonstrated superior performance, achieving an accuracy of 0.90. This improvement can be attributed to the model's ability to integrate spatial information alongside spectral features, enhancing its capability to accurately identify volcanic clouds.

The integration of the VGG16-UNet model with the high temporal resolution of SEVIRI enables continuous observation and tracking of volcanic clouds from their formation during an eruption to their dispersion into the atmosphere. This marks a significant step towards developing a versatile model that can be applied to monitor volcanic activity globally. To enhance the model's generalizability, future efforts should include images from diverse volcanic regions in the training dataset, ensuring adaptability across different volcanic environments. This process ensures that the model becomes adaptable and can effectively generalize across diverse volcanoes. This approach is ideal for rapidly analyzing larger volumes of data in near-real-time scenarios, and its application can provide crucial support to operational monitoring centers, contributing to more effective management of volcanic ash clouds.

The application of this technique in near-real-time scenarios can provide invaluable support to operational monitoring centers, enabling more effective management of volcanic ash clouds and mitigating potential risks associated with volcanic eruptions. Overall, our study underscores the importance of leveraging advanced computational techniques for enhancing volcanic cloud monitoring and management efforts.

Funding

CRediT authorship contribution statement

Federica Torrisi: Writing – original draft, Software, Methodology, Data curation, Conceptualization. **Claudia Corradino:** Writing – review & editing, Writing – original draft, Methodology, Conceptualization. **Simona Cariello:** Visualization, Formal analysis. **Ciro Del Negro:** Writing – review & editing, Supervision, Resources, Methodology.

Declaration of competing Interest

The authors declare that they have no known competing financial interests or personal relationships that could have appeared to influence the work reported in this paper.

Data availability

Data will be made available on request.

Acknowledgments

References

Amato, E., Corradino, C., Torrisi, F., Del Negro, C., 2022. Combined use of satellite data and machine learning for detecting, measuring, and monitoring active lava flows at Etna Volcano [Other]. Geophysics. https://doi.org/10.1002/essoar.10509929.1.

Amato, E., Corradino, C., Torrisi, F., Del Negro, C., 2023. A deep convolutional neural network for detecting volcanic thermal anomalies from satellite images. Remote Sens. 15 (15) https://doi.org/10.3390/rs15153718. Articolo 15.

Aminou, D., 2002. MSG's SEVIRI instrument. ESA Bull. 111.

Ardid, A., Dempsey, D., Caudron, C., Cronin, S., Kennedy, B., Girona, T., Roman, D., 2023. Generalized Eruption Forecasting Models using Machine Learning Trained on Seismic Data from 24 Volcanoes.

Calvari, S., Nunnari, G., 2022. Comparison between automated and manual detection of lava fountains from fixed monitoring thermal cameras at Etna Volcano, Italy. Remote Sens. 14 (10) https://doi.org/10.3390/rs14102392. Articolo 10.

Campbell, N.A., 1996. The decorrelation stretch transformation. Int. J. Remote Sens. 17 (10), 1939–1949.

Chen, W.R., Zhao, L.R., 2015. Review – Volcanic ash and its influence on aircraft engine components. Proc. Eng. 99, 795–803. https://doi.org/10.1016/j.proeng.2014.12.604.

Corradino, C., Amato, E., Torrisi, F., Calvari, S., Del Negro, C., 2021. Classifying major explosions and paroxysms at stromboli volcano (Italy) from space. Remote Sens. 13 (20) https://doi.org/10.3390/rs13204080. Articolo 20.

Corradino, C., Ramsey, M.S., Pailot-Bonnetat, S., Harris, A.J.L., Del Negro, C., 2023. Detection of Subtle thermal anomalies: deep learning applied to the ASTER global volcano dataset. IEEE Trans. Geosci. Remote Sens. 61, 1–15. https://doi.org/10.1109/TGRS.2023.3241085.

Dempsey, D.E., Kempa-Liehr, A.W., Ardid, A., Li, A., Orenia, S., Singh, J., Cronin, S.J., 2022. Evaluation of short-term probabilistic eruption forecasting at Whakaari, New Zealand. Bull. Volcanol. 84 (10), 91.

Durant, A.J., Rose, W.I., Sarna-Wojcicki, A.M., Carey, S., Volentik, A.C.M., 2009. Hydrometeor-enhanced tephra sedimentation: constraints from the 18 May 1980 eruption of Mount St. Helens. J. Geophys. Res. Solid Earth 114 (B3). https://doi.org/10.1029/2008JB005756, 2008JB005756.

van Dyk, D.A., Meng, X.-L., 2001. The art of data augmentation. J. Comput. Graph. Stat. 10 (1), 1–50. https://doi.org/10.1198/10618600152418584.

Gilbert, J.S., Sparks, R.S.J., 1998. Future research directions on the physics of explosive volcanic eruptions. Geol. Soc. Lond. Spec. Publ. 145 (1), 1–7. https://doi.org/10.1144/GSL.SP.1996.145.01.01.

Gudmundsson, G., 2011. Respiratory health effects of volcanic ash with special reference to Iceland. A review. Clin. Respir. J. 5 (1), 2–9. https://doi.org/10.1111/j.1752-699X.2010.00231.x.

Hunton, D.E., Viggiano, A.A., Miller, T.M., Ballenthin, J.O., Reeves, J.M., Wilson, J.C., Lee, S.-H., Anderson, B.E., Brune, W.H., Harder, H., Simpas, J.B., Oskarsson, N., 2005. In-situ aircraft observations of the 2000 Mt. Hekla volcanic cloud: composition and chemical evolution in the Arctic lower stratosphere. J. Volcanol. Geotherm. Res. 145 (1), 23–34. https://doi.org/10.1016/j.jvolgeores.2005.01.005.

Ishigami, A., Kikuchi, Y., Iwasawa, S., Nishiwaki, Y., Takebayashi, T., Tanaka, S., Omae, K., 2008. Volcanic sulfur dioxide and acute respiratory symptoms on Miyakejima island. Occup. Environ. Med. 65 (10), 701–707. https://doi.org/10.1136/oem.2007.033456.

Kanaeva, I., Ivanova, J., 2021. Road pavement crack detection using deep learning with synthetic data. IOP Confer. Ser.: Mater. Sci. Eng. 1019 https://doi.org/10.1088/1757-899X/1019/1/012036, 012036.

Kingma, D.P., Ba, J., 2017. Adam: A method for stochastic optimization (arXiv: 1412.6980). arXiv. https://doi.org/10.48550/arXiv.1412.6980.

Li, X., Xiong, H., Li, X., Wu, X., Zhang, X., Liu, J., Bian, J., Dou, D., 2022. Interpretable deep learning: Interpretation, interpretability, trustworthiness, and beyond. Knowl. Inf. Syst. 64 (12), 3197–3234. https://doi.org/10.1007/s10115-022-01756-8.

Nayak, R., 2022. Focal Loss: A Better Alternative for Cross-Entropy. Medium. https://towardsdatascience.com/focal-loss-a-better-alternative-for-cross-entropy-1d073d92d075.

Pavolonis, M.J., Sieglaff, J., Cintineo, J., 2018. Automated detection of explosive volcanic eruptions using satellite-derived cloud vertical growth rates. Earth Space Sci. 5 (12), 903–928. https://doi.org/10.1029/2018EA000410.

Petracca, I., De Santis, D., Picchiani, M., Corradini, S., Guerrieri, L., Prata, F., Merucci, L., Stelitano, D., Del Frate, F., Salvucci, G., Schiavon, G., 2022. Volcanic cloud detection using Sentinel-3 satellite data by means of neural networks: The Raikoke 2019 eruption test case. Atmos. Meas. Tech. 15 (24), 7195–7210. https://doi.org/10.5194/amt-15-7195-2022.

Piontek, D., Bugliaro, L., Kar, J., Schumann, U., Marenco, F., Plu, M., Voigt, C., 2021. The new volcanic ash satellite retrieval VACOS using MSG/SEVIRI and artificial neural networks: 2. Validation. Remote Sens. 13 (16), 3128.

Prata, A.J., 1989a. Infrared radiative transfer calculations for volcanic ash clouds. Geophys. Res. Lett. 16 (11), 1293–1296. https://doi.org/10.1029/GL016i011p01293.

Prata, F., 1989b. Observations of volcanic ash clouds in the 10-12 ??m window using AVHRR/2 data. Intern. J. Remote Sens. - Int J Remote Sens 10, 751–761. https://doi.org/10.1080/01431168908903916.

Prata, F., Lynch, M., 2019. Passive earth observations of volcanic clouds in the atmosphere. Atmosphere 10 (4). https://doi.org/10.3390/atmos10040199. Articolo 4.

Pyle, D., 1998. Sparks, R. S. J., Bursik, M. I., Carey, S. N., Gilbert, J. S., Glaze, L. S., Sigurdsson, H. & Woods, A. W. 1997. Volcanic Plumes. xv + 574 pp. Chichester, New York, Weinheim, Brisbane, Singapore, Toronto: John Wiley & Sons. Price £85.00 (hard covers). ISBN 0 471 93901 3. Geol. Mag. 135 (1), 143–158. https://doi.org/10.1017/S0016756897278258.

Ronneberger, O., Fischer, P., Brox, T., 2015. U-Net: convolutional networks for biomedical image segmentation (arXiv:1505.04597). arXiv. https://doi.org/10.48550/arXiv.1505.04597.

Rose, W., Delene, D., Schneider, D., Bluth, G., Sprod, I., Krueger, A., Mckee, C., Davies, H., Ernst, G., 1995. Ice in the 1994 Rabaul eruption cloud: implications for volcano hazard and atmospheric effects. Nature 375, 477–479. https://doi.org/10.1038/375477a0.

Sawada, Y., 1987. Study on analyses of volcanic eruptions based on eruption cloud image data obtained by the geostationary meteorological satellite (GMS). Tech. Report Meteorol. Res. Inst. 22, 1–335.

Sawada, Y., 1996. Detection of explosive eruptions and regional tracking of volcanic ash clouds with Geostationary Meteorological Satellite (GMS) (A c. Di). In: Scarpa, R., Tilling, R.I. (Eds.), Monitoring and Mitigation of Volcano Hazards. Springer, pp. 299–314. https://doi.org/10.1007/978-3-642-80087-0_9.

Scollo, S., Prestifilippo, M., Spata, G., D'Agostino, M., Coltelli, M., 2009. Monitoring and forecasting Etna volcanic plumes. Nat. Hazards Earth Syst. Sci. 9 (5), 1573–1585. https://doi.org/10.5194/nhess-9-1573-2009.

Self, S., 2006. The effects and consequences of very large explosive volcanic eruptions. Philos. Trans. R. Soc. A Math. Phys. Eng. Sci. 364 (1845), 2073–2097.

Shelhamer, E., Long, J., Darrell, T., 2017. Fully convolutional networks for semantic segmentation. IEEE Trans. Pattern Anal. Mach. Intell. 39 (4), 640–651.

Simonyan, K., Zisserman, A., 2014. Very Deep Convnets for Large-scale Image Recognition. Computing Research Repository.

Tomar, N., 2021. What is UNET? Analytics Vidhya. https://medium.com/analytics-vidhya/what-is-unet-157314c87634.

Torrisi, F., 2022. Automatic detection of volcanic ash clouds using MSG-SEVIRI satellite data and machine learning techniques. Il Nuovo Cimento C 45 (4). Articolo 4.

Torrisi, F., Amato, E., Corradino, C., Mangiagli, S., Del Negro, C., 2022. Characterization of volcanic cloud components using machine learning techniques and SEVIRI infrared images. Sensors 22 (20). https://doi.org/10.3390/s22207712. Articolo 20.

Torrisi, F., Amato, E., Corradino, C., Del Negro, C., 2023. The FastVRP automatic platform for the thermal monitoring of volcanic activity using VIIRS and SLSTR sensors: FastFRP to monitor volcanic radiative power. Ann. Geophys. 65 (6), 1. https://doi.org/10.4401/ag-8823.

Webley, P.W., Dehn, J., Lovick, J., Dean, K.G., Bailey, J.E., Valcic, L., 2009. Near-real-time volcanic ash cloud detection: experiences from the Alaska Volcano Observatory. J. Volcanol. Geotherm. Res. 186 (1), 79–90. https://doi.org/10.1016/j.jvolgeores.2009.02.010.

Weng, Y., Zhou, T., Li, Y., Qiu, X., 2019. NAS-Unet: neural architecture search for medical image segmentation. IEEE Access 7, 44247–44257. https://doi.org/10.1109/ACCESS.2019.2908991.

Williams-Jones, G., Rymer, H., 2015. Chapter 57—Hazards of Volcanic Gases (A c. Di). In: Sigurdsson, H. (Ed.), The Encyclopedia of Volcanoes, Second edition. Academic Press, pp. 985–992. https://doi.org/10.1016/B978-0-12-385938-9.00057-2.

Wilson, T.M., Stewart, C., Sword-Daniels, V., Leonard, G.S., Johnston, D.M., Cole, J.W., Wardman, J., Wilson, G., Barnard, S.T., 2012. Volcanic ash impacts on critical infrastructure. Phys. Chem. Earth, Parts A/B/C 45–46, 5–23. https://doi.org/10.1016/j.pce.2011.06.006.

Zhang, Q., Wu, Y.N., Zhu, S.C., 2018. Interpretable convolutional neural networks. In: *Proceedings of the IEEE conference on computer vision and pattern recognition*, pp. 8827–8836. 10.1109/CVPR.2018.00920.